



An alkali metal thermoelectric converter hybridized with a Brayton heat engine: Parametric design strategies and energetic optimization

Wanli Peng^{a, b}, Julian Gonzalez-Ayala^{b, c}, Juncheng Guo^d, Jincan Chen^{a, *}, Antonio Calvo Hernández^{b, c, **}

^a Department of Physics, Xiamen University, Xiamen, 361005, People's Republic of China

^b Departamento de Física Aplicada, Universidad de Salamanca, 37008, Salamanca, Spain

^c Instituto de Física Fundamental y Matemáticas, Universidad de Salamanca, 37008, Salamanca, Spain

^d College of Physics and Information Engineering, Fuzhou University, Fuzhou, 350116, People's Republic of China

ARTICLE INFO

Article history:

Received 9 January 2020

Received in revised form

3 March 2020

Accepted 5 March 2020

Available online 14 March 2020

Handling editor: Bin Chen

Keywords:

Alkali metal thermoelectric converter

Brayton heat engine

Hybridization

Parametric strategy

Multiobjective optimization

ABSTRACT

A model for a novel integrating system consisting of an alkali metal thermoelectric converter and a non-recuperative irreversible Brayton heat engine is presented. The efficiency and power output density of the overall system is analyzed at light of the main characteristic losses in each subsystem: the thickness of the electrolyte, the current density of the converter, and the internal losses of the Brayton cycle coming from the compressor and turbine. A detailed study on the behavior of the overall maximum power and maximum efficiency regimes is also presented. An analysis on compromise performance regimes from multi-objective and multi-parametric optimization techniques based on the Pareto front, for both the subsystems and the overall system, enhance the obtained results. The numerical results of the present model are compared with those of alkali metal thermoelectric converter working alone and with other different existing hybrid models. It is found that the exhaust heat discharged by the converter can be efficiently utilized by an irreversible Brayton heat engine. So, the maximum efficiency and maximum power output density of the present model attain 41.7% and $116 \times 10^3 \text{ W/m}^2$ which increase about 44.8% and 158% compared to the values of the alkali metal thermoelectric converter working alone and 20.5% and 80.4% when compared with a hybridized configuration including a thermoelectric energy converter.

© 2020 Elsevier Ltd. All rights reserved.

1. Introduction

The alkali metal thermoelectric converter (AMTEC) using sodium as the working substance has been used as an efficient device to directly convert heat into electrical energy. It is mainly comprised by several connected β -alumina solid electrolyte (BASE) tubes. The BASE acts as selective barrier to the medium due to its higher ion conductivity in comparison with its electronic conductivity. The thermodynamic pressure and temperature differences across BASE cause ionization of sodium atoms at the hot side. Sodium ions diffuse through the BASE to the cathode side while isolated electrons are collected at the anode and they circulate

through the external circuit, producing electrical work on the external load. Finally, electrons and sodium ions recombine at the surface between the BASE and the cathode. AMTECs have many inherent advantages such as the absence of moving parts, reliability, absence of noise, competitive manufacturing costs, and higher efficiency (20%–40%) when compared with other thermoelectric devices.

From a thermal point of view, an AMTEC device works between a high-temperature area (ranging between 900 K and 1300 K) which acts as an evaporator for the high pressure sodium vapor entering the anode, and a low-temperature area (ranging between 400 K and 800 K) acting as a condenser for the low pressure sodium vapor exiting the cathode. From an energetic perspective, the temperature of the condenser plays a key role since at that high temperature heat is released directly to the ambient, thus provoking a large environmental thermal damage. So many efforts have been devoted to overcome this situation by minimizing the heat release to the ambient and/or use lower temperatures in the

* Corresponding author.

** Corresponding author. Departamento de Física Aplicada, Universidad de Salamanca, 37008, Salamanca, Spain.

E-mail addresses: jchen@xmu.edu.cn (J. Chen), anca@usal.es (A.C. Hernández).

Nomenclature	
A	overall area, m^2
B	a coefficient, $AK^{1/2}/P_a/m^2$
c_C	thermal capacitance rate, J/K
c_P	molar specific heat, $J/mol/K$
c_L	thermal conductance, J/K
D	thickness, m
F	Faraday constant, C/mol
G	pressure losses geometric factor
J	current density, A/m^2
L	latent heat, J/g
M	molecular weight, g/mol
p	POD, W/m^2
p_1	pressure of process 4-1, P_a
p_2	pressure of process 2-3, P_a
P	power output, W
p_{sat}	saturation vapor pressure, P_a
Δp_{cd}	pressure loss, P_a
q_H	heat flow from the heat source, W
q_C	heat flow from the condenser, W
q_0	heat flow from the BHE, W
q_L	heat leak rate, W
R	gas constant, $J/mol/K$
r_p	pressure ratio
T_H	evaporator temperature, K
T_C	condenser temperature, K
T_0	environment temperature, K
U	heat transfer coefficient, $J/K/m^2$
V	voltage output, V
V_{ac}	over potential difference, V
V_R	ionic BASE voltage, V
x	adiabatic temperature ratio
z	radiation reduction factor
<i>Greek symbols</i>	
ε	effectiveness
γ	adiabatic coefficient
η	efficiency
η_{12}	isentropic compression efficiency
η_{34}	isentropic expansion efficiency
μ	a coefficient, m^2
σ	Stefan-Boltzmann constant, $W/m^2/K^4$
<i>Subscripts</i>	
A/B	AMTEC/BHE C/O hot/cold side heat exchanger
E	electrode
max	maximum
<i>Abbreviations</i>	
AMTEC	alkali metal thermoelectric converter
BASE	β -alumina solid electrolyte
BHE	Brayton heat engine
ME	maximum efficiency
MPOD	maximum power output density
POD	power output density
TEG	thermoelectric generator
AR	absorption refrigerator

condenser: For example, [Lodhi and Daloglu \(2000\)](#) optimized the efficiency by changing some geometrical dimensions of the device so that the condenser temperature is 623 K; [Underwood et al. \(1992\)](#) identified a new concept for an AMTEC vapor-vapor series connected cell where condenser temperature is 500 K; [El-Genk and Tournier \(2002\)](#) reported that the potassium converters (560 K) exhibit a temperature 90 K lower than the sodium converter (650 K) near the optimum condenser temperature.

Another strategy to increase the AMTEC device efficiency is to recycle the heat waste released by the condenser. It is noteworthy to mention some coupling devices where the AMTEC is coupled to an additional bottoming power system: [Wang et al. \(2019\)](#) established an integrating system composed of an AMTEC and an absorption refrigerator (AR) and obtained the maximum efficiencies of the stand-alone AMTEC and hybrid system, which are 26.57% and 39.24%, respectively. [Wu et al. \(2019\)](#) proposed a new hybrid system by the coupling of an AMTEC with a Triple-effect AR which utilizes the condensation heat of the AMTEC as the heat source of an absorption refrigerator (with a maximum value of the exergetic efficiency of 42.7%). Also, [Wu et al. \(2017\)](#) developed the model of the AMTEC/TEG hybrid system consisting of AMTEC and thermoelectric generator (TEG) with the overall efficiency 31.3% higher than that of the single AMTEC. Later, [Peng et al. \(2019a\)](#) improved the analysis of the AMTEC/TEG hybrid system by considering explicitly the thickness of the AMTEC-electrolyte and obtaining the maximum overall efficiency 34.6% higher than that of both the single AMTEC and the AMTEC/TEG hybrid system previously analyzed by [Wu et al. \(2017\)](#).

On the other side, the well-known Brayton cycle has been widely used in gas-turbine power plants and aircraft propulsion systems ([Horlock, 2003](#)) with different optimization criteria ([Cheng, 1999](#)), and regenerative and isentropic losses ([Zhang et al.,](#)

[2006](#); [Sánchez-Organ et al., 2010](#)). More recent studies include applications to regenerative and non-regenerative models with different arrangements for multi-compression and multi-expansion processes ([Bontempo and Manna, 2019](#)), different working fluids including supercritical carbon dioxide ([González-Portillo et al., 2019](#)), and hybridized power plants with solar energy ([Santos et al., 2016](#)) or biomass ([Durante et al., 2017](#)) and energy storage ([Guo et al., 2016](#)). Its wide versatility, in the used working fluids, multi-step arrangements, capacity of regeneration, and combustion processes, allows its application in a broad variety of energy sources. Also, its main internal irreversibilities are well characterized in terms of the compressor and turbine isentropic efficiencies and heat leak between the external heat baths. However, to the best of our knowledge, the possibility of its use as a bottoming cycle to recycle the heat waste coming from an AMTEC system has not been explored. Indeed, the BHE requires pressurized working fluid flow with enough grade heat for operation. As noted above AMTEC works between 900 K and 1300 K in the hot side (evaporator) and 400 K–800 K in the cold side (condenser). This range of temperatures seems to be enough to drive a one-step and non-recuperative BHE with small pressure ratios.

The aim of this paper is to quantitatively analyze the energetic performance of a coupled system composed of an AMTEC and an irreversible and non-regenerative Brayton heat engine (BHE). In particular, the first goal is the analysis of the needed matching conditions of both subsystems, taken into account the main irreversibilities of each one while the second goal is to analyze the global optimum performance regimes in terms of the characteristic parameters of each subsystem. The simulated optimization study will be complemented by using multi-objective and multi-parametric optimization techniques based on the Pareto front for the energetic efficiency and on the optimal set of physically

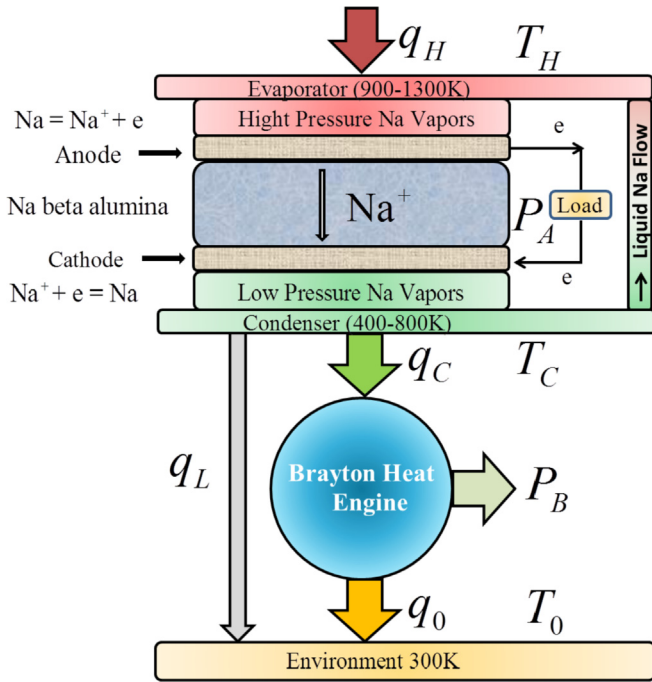


Fig. 1. The diagram of an AMTEC-BHE integrating system.

accessible states.

2. The AMTEC-BHE coupling

The AMTEC-BHE hybrid model used in this work is sketched in Fig. 1. The AMTEC is divided into two regions, where one is a high temperature T_H region (900–1300 K) with an evaporator (anode) and the other is a low temperature T_C region (400–800 K) with a condenser (cathode) by the BASE (Peng et al., 2018; Wu et al., 2018; Lodhi et al., 2001). The Brayton cycle is operated between the environment temperature T_0 and the temperature T_C .

In Fig. 1, P_A and P_B denote the power outputs of the AMTEC and the BHE, respectively; q_H is the heat flow from the heat bath to the AMTEC; q_C and q_0 are, respectively, the heat flows from the AMTEC to the BHE and from the BHE to the environment; and q_L is the heat leak rate from the condenser of the AMTEC to the surroundings.

2.1. Power output and efficiency of the AMTEC

An AMTEC is a static device for the conversion of heat to electricity as heat engine. Peng et al. (2018) derived the expressions of the power output and efficiency of the AMTEC in detail. The power output P_A and efficiency η_A read as

$$P_A = J \cdot A_E \cdot V \quad (1)$$

and

$$\eta_A = \frac{P_A}{q_H} = \frac{J \cdot V}{J \cdot V + J \cdot M \cdot L / F + J \cdot c_p \cdot (T_H - T_C) \cdot M / F + \sigma \cdot (T_H^4 - T_C^4) / z}, \quad (2)$$

where J indicates the current density of the AMTEC, c_p is the molar specific heat, L and M denote, respectively, the vaporization latent heat and the molecular weight of sodium, σ denotes the Stefan-Boltzmann constant, z is a radiation reduction factor, F is Faraday

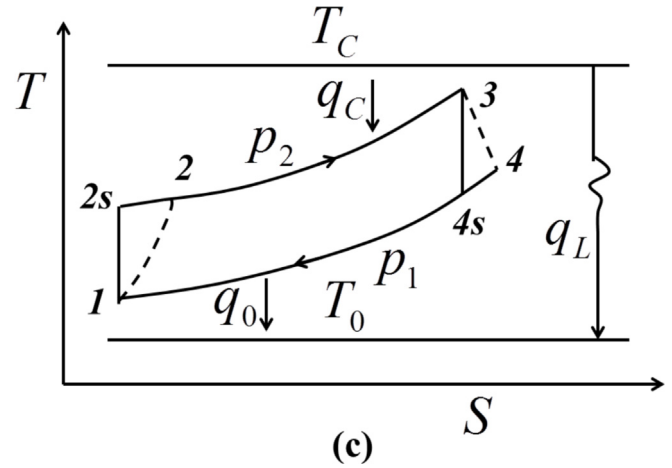


Fig. 2. The T-S diagram of a BHE.

$$q_C = c_C \cdot \epsilon_C \cdot (T_C - T_2) = c_C \cdot (T_3 - T_2) \quad (3)$$

Table 1

The values of some parameters used in the integrating system (Wu et al., 2010; Cheng, 1999; Tournier et al., 1997).

T_H (K)	1300
T_0 (K)	300
σ (W/m ² /K ⁴)	5.67×10^{-8}
$B(A\sqrt{R}/Pa/m^2)$	90
μ (m ²)	10^7
F (C/mol)	9685
L (J/g)	4480
M (g/mol)	23
G	10
R (J/mol/K)	8.314
z	50
c_p (J/mol/K)	30
ϵ_C	0.95
ϵ_0	0.99
η_{12}	0.85
η_{34}	0.9
c_L/c_C	0.02

constant, A_E corresponds to the area on the BASE electrode, and V indicates the voltage output (see Appendix A).

2.2. Power output and efficiency of the BHE

The temperature-entropy diagram of a non-regenerative irreversible BHE with one compressor and one turbine, operated between the heat bath at temperature T_C and the heat sink at temperature T_0 , is shown in Fig. 2. The model incorporates the main basic irreversibilities of real gas-turbine power plants: a) the external irreversibilities coming from the working fluid to external heat baths, b) the internal irreversibilities coming from non-isentropic expansion and compression processes in the turbine and compressor, respectively, and c) the heat leak between the two external heat baths at T_C and T_0 . Pressure drops in the heater and cooler are not considered. In Fig. 2: Isobaric processes 2–3 with pressure p_2 and 4–1 with pressure p_1 account for the constant-pressure heat addition and heat release transfers. Steps 1–2s and 3–4s stand for the isentropic compression and expansion processes, while steps 1–2 and 3–4 are the irreversible adiabatic processes induced by the real compressor and turbine, respectively.

Thus, the involved heat flows between the heat reservoirs at temperatures T_C and T_0 and the working substance of the BHE can be written as and

$$q_0 = c_C \cdot \varepsilon_0 \cdot (T_4 - T_0) = c_C \cdot (T_4 - T_1), \tag{4}$$

respectively, where c_C is the thermal capacitance rate, $\varepsilon_{C/0}$ is the effectiveness of the hot/cold side for counterflow heat exchangers. These coefficients can be defined as (Cheng, 1999)

$$\varepsilon_C = 1 - \exp\left(-\frac{U_C \cdot A_C}{c_C}\right) \tag{5}$$

and

$$\left\{ \begin{aligned} T_1 &= \frac{a_1 \cdot x + a_2}{a_3 \cdot x^2 + a_4 \cdot x + a_5} \\ T_2 &= \frac{a_1 \cdot x + a_2}{a_3 \cdot x^2 + a_4 \cdot x + a_5} \cdot (1/\eta_{12}) \cdot (x - 1 + \eta_{12}) \\ T_3 &= \varepsilon_C \cdot T_C + \frac{a_1 \cdot x + a_2}{a_3 \cdot x^2 + a_4 \cdot x + a_5} \cdot (1 - \varepsilon_C) \cdot (1/\eta_{12}) \cdot (x - 1 + \eta_{12}) \\ T_4 &= \frac{a_1 \cdot x + a_2}{a_3 \cdot x^2 + a_4 \cdot x + a_5} \cdot \frac{1}{(1 - \varepsilon_0)} - \frac{\varepsilon_0 \cdot T_0}{1 - \varepsilon_0} \end{aligned} \right. \tag{11}$$

$$\varepsilon_0 = 1 - \exp\left(-\frac{U_0 \cdot A_0}{c_C}\right), \tag{6}$$

$$\eta_{34} = \frac{T_3 - T_4}{T_3 - T_{4s}}, \tag{9}$$

respectively. According to the isentropic character of processes 1–2s and 3–4s, one has the following relation (Guo et al., 2016)

$$\frac{T_{2s}}{T_1} = \frac{T_3}{T_{4s}} = \left(\frac{p_2}{p_1}\right)^{\frac{\gamma-1}{\gamma}} = r_p^{\frac{\gamma-1}{\gamma}} = x, \tag{10}$$

where $r_p = \frac{p_2}{p_1}$ denotes the pressure ratio of two isobaric processes, γ is the adiabatic coefficient, and x stands for the adiabatic temperature ratio.

From Eqs. (3), (4) and (8)-(10), one can get

where

$$\left\{ \begin{aligned} a_1 &= -(1/\eta_{34}) \cdot [\varepsilon_0 / (1 - \varepsilon_0)] \cdot T_0 + \varepsilon_C \cdot (1 - 1/\eta_{34}) \cdot T_C \\ a_2 &= -\varepsilon_C \cdot T_C \\ a_3 &= -(1/\eta_{12}) \cdot (1 - 1/\eta_{34}) \cdot (1 - \varepsilon_C) \\ a_4 &= -(1 - \varepsilon_C) \cdot (1 - 1/\eta_{12}) \cdot (1 - 1/\eta_{34}) + (1 - \varepsilon_C) / \eta_{12} - 1/\eta_{34} \cdot [1 / (1 - \varepsilon_0)] \\ a_5 &= (1 - 1/\eta_{12}) \cdot (1 - \varepsilon_C) \end{aligned} \right. \tag{12}$$

where $A_{C/0}$ is the area of the hot/cold-end heat exchanger and $U_{C/0}$ is the overall heat transfer coefficient.

For the heat leak q_L , we assume the usual linear dependence on the involved temperatures. Then, it can be written as

$$q_L = c_L \cdot (T_C - T_0), \tag{7}$$

where c_L denotes the corresponding thermal conductance.

The isentropic compression efficiency η_{12} and isentropic expansion efficiency η_{34} can be expressed as (Horlock, 2003; Cheng, 1999; Zhang et al., 2006; Sánchez-Orgaz et al., 2010)

$$\eta_{12} = \frac{T_{2s} - T_1}{T_2 - T_1} \tag{8}$$

and

The power output P_B and efficiency η_B of the BHE are displayed as

$$\begin{aligned} P_B &= q_C - q_0 = c_C \cdot (T_3 - T_2 - T_4 + T_1) \\ &= c_C \cdot \left[\varepsilon_C \cdot T_C - \varepsilon_C \cdot (x - 1 + \eta_{12}) \cdot \left(\frac{1}{\eta_{12}}\right) \right. \\ &\quad \left. \cdot \left(\frac{a_1 \cdot x + a_2}{a_3 \cdot x^2 + a_4 \cdot x + a_5}\right) - \frac{\varepsilon_0}{1 - \varepsilon_0} \cdot \left(\frac{a_1 \cdot x + a_2}{a_3 \cdot x^2 + a_4 \cdot x + a_5} - T_0\right) \right] \end{aligned} \tag{13}$$

and

$$\eta_B = \frac{P_B}{q_C + q_L} = \frac{c_C \cdot \left[\varepsilon_C \cdot T_C - (x - 1 + \eta_{12}) \cdot \left(\frac{\varepsilon_C}{\eta_{12}} \right) \cdot \left(\frac{a_1 \cdot x + a_2}{a_3 \cdot x^2 + a_4 \cdot x + a_5} \right) - \frac{\varepsilon_0}{1 - \varepsilon_0} \cdot \left(\frac{a_1 \cdot x + a_2}{a_3 \cdot x^2 + a_4 \cdot x + a_5} - T_0 \right) \right]}{c_C \cdot \varepsilon_C \cdot \left[T_C - \left(\frac{x - 1 + \eta_{12}}{\eta_{12}} \right) \cdot \left(\frac{a_1 \cdot x + a_2}{a_3 \cdot x^2 + a_4 \cdot x + a_5} \right) \right] + c_L \cdot (T_C - T_0)} \quad (14)$$

2.3. Power output and efficiency of the hybridized system

According to Eqs. (1)–(5) and (13) and (14), one can obtain the power output P and efficiency η of the coupled AMTEC-BHE system as

$$P = P_A + P_B = q_H - q_L - q_0 = J \cdot A_E \cdot V + c_C \cdot \left[\varepsilon_C \cdot T_C - \varepsilon_C \cdot (x - 1 + \eta_{12}) \cdot \left(\frac{1}{\eta_{12}} \right) \cdot \left(\frac{a_1 \cdot x + a_2}{a_2 \cdot x^2 + a_4 \cdot x + a_5} \right) - \frac{\varepsilon_0}{1 - \varepsilon_0} \cdot \left(\frac{a_1 \cdot x + a_2}{a_2 \cdot x^2 + a_4 \cdot x + a_5} - T_0 \right) \right] \quad (15)$$

and

$$\eta = \frac{P}{q_H} = \eta_A + \eta_B \cdot (1 - \eta_A) \quad (16)$$

3. Results

All results presented below have been obtained with Mathematica self-written code starting with analytical expressions in section 2 and then solving the parametric optimization. A close inspection of Eqs. (2), (3), and (13)–(16) can show that the main energetic properties of the whole AMTEC-BHE system, such as the power output and efficiency. They depend on a set of parameters accounting for each subsystem, the coupling condition at the condenser (the temperature T_C bounds the heat absorbed by the Brayton cycle), and the parameter ratio c_C/A_E which can be obtained from conservation of energy for the whole system as $P_A + P_B = q_H - q_L - q_0$. A number of representative parameters listed in Table 1 have been fixed. It has been checked that the qualitative behaviors of the system are similar for other set of values. Because T_C is dependent on D (appendix A), the independent variables have only J , D , and x . A first discussion is stems from considering a constant D . Later-on, the optimal performance analysis for different

D -values will be shown.

3.1. Optimum performance for a given D

By using Eqs. 15 and 16, and (A1)–(A4), the power output density (POD) $p = P/A_E$ and efficiency η of the overall system can be calculated for different values of x and J , as displayed in Fig. 3(a) and (b), respectively. Fig. 3 shows that p and η exhibit their respective maxima, 1.42×10^4 W/m² and 0.352, respectively, at different optimum values [x_p at the maximum POD (MPOD) and x_η at the maximum efficiency (ME)] of x and (J_p and J_η) of J . It should be stressed that the ME of the integrating system increases about 12.5% and 1.73% compared with that of the AMTEC-TEG hybrid systems in Refs. (Wu et al., 2017; Peng et al., 2019a), respectively.

Similarly, the influence of J on both p and η are displayed in Fig. 4 (a), where P_η and η_p denote the POD at the ME (η_{max}) and the efficiency at the MPOD (p_{max}), respectively. It is clearly seen from Fig. 4 (a) that for a given D , there exist a MPOD p_{max} and a ME η_{max} , and the corresponding optimum values J_η and J_p of J are, respectively, equal to 6.31×10^3 A/m² and 3.16×10^4 A/m². In Fig. 4 (a), it is also clear that both p and η in the region of $J < J_\eta$ increase as J increases, while both p and η in the region of $J > J_p$ decrease as J increases. It indicates that both the ranges of $J < J_\eta$ and of $J > J_p$ are not optimal for the overall system. Thus, the optimum region of J is given by

$$J_\eta \leq J \leq J_p \quad (17)$$

We can further obtain the $\eta \sim p$ curve, as shown in Fig. 4 (b), where the characteristic loop behavior of the power versus efficiency curve of the system is clearly observed. Therefore, the optimal regions of p and η for a given value of D are given by

$$p_\eta \leq p \leq p_{max} \quad (18)$$

and

$$\eta_p \leq \eta \leq \eta_{max} \quad (19)$$

Regarding Fig. 4, two points are stressed. First, a closer

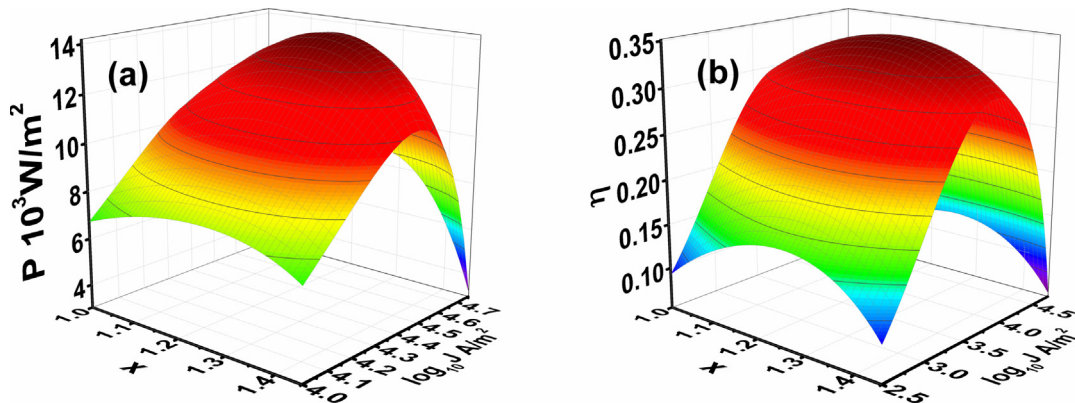


Fig. 3. (a) p and (b) η as functions of x and J for $D = 3.16 \times 10^{-4}$ m.

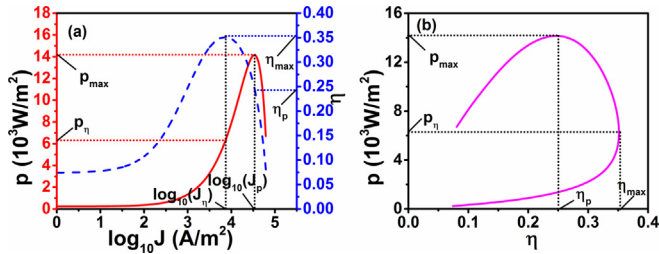


Fig. 4. (a) p and η as functions of J , where x_p and x_{η} are the values of x at the MPOD and ME, respectively. (b) The p versus η curve. $D = 3.16 \times 10^{-4} \text{ m}$ is used.

inspection of Fig. 4a clearly shows that there is a long flat tail for low J -values, while the physical region after the maximum value is strongly decreasing and up to some finite upper value of J . Second, Fig. 4b indicates the power-efficiency characteristic curve and is directly obtained by Eqs. (15) and (16), where both J and x have been optimized. In other words, each point in Fig. 4b is a state of the power and efficiency at the optimized J and x values. The resulting power-efficiency curve has a loop-like behavior, which is as a “signature” of a true, realistic irreversible heat engine with the maximum efficiency and maximum power states close each other but non coincident.

3.2. Dependence of the optimum performance on D

Until now, the thickness of the electrolyte membrane D is taken as a fixed value. However, it plays a key role in the optimized regimes for the power output and efficiency. In this section, we will

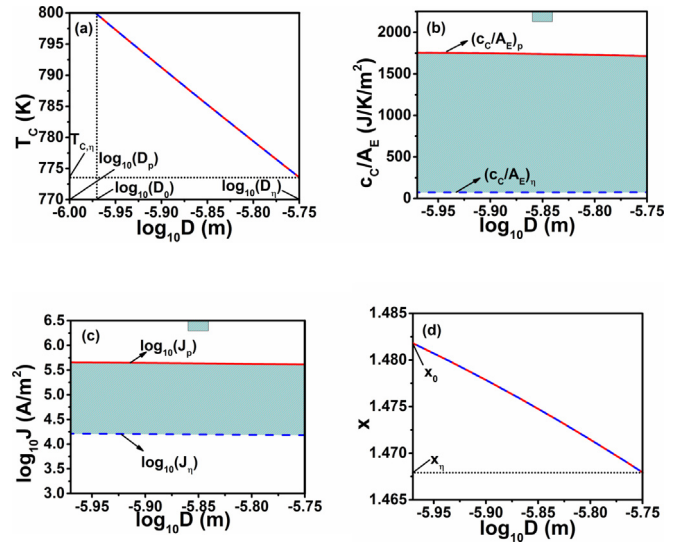


Fig. 6. (a) T_c , (b) c_c/A_E , (c) J , and (d) x as functions of D .

discuss the influence of D on the systemic performance.

By using Eqs. (15) and (16), p_{opt} and η_{opt} can be obtained for different values of D , as shown in Fig. 5, where J and x have been taken as those values that optimize POD and efficiency. Note how power output density and efficiency in Fig. 5 (red solid color) exhibits a clear parabolic characteristic behavior in terms of D . It is

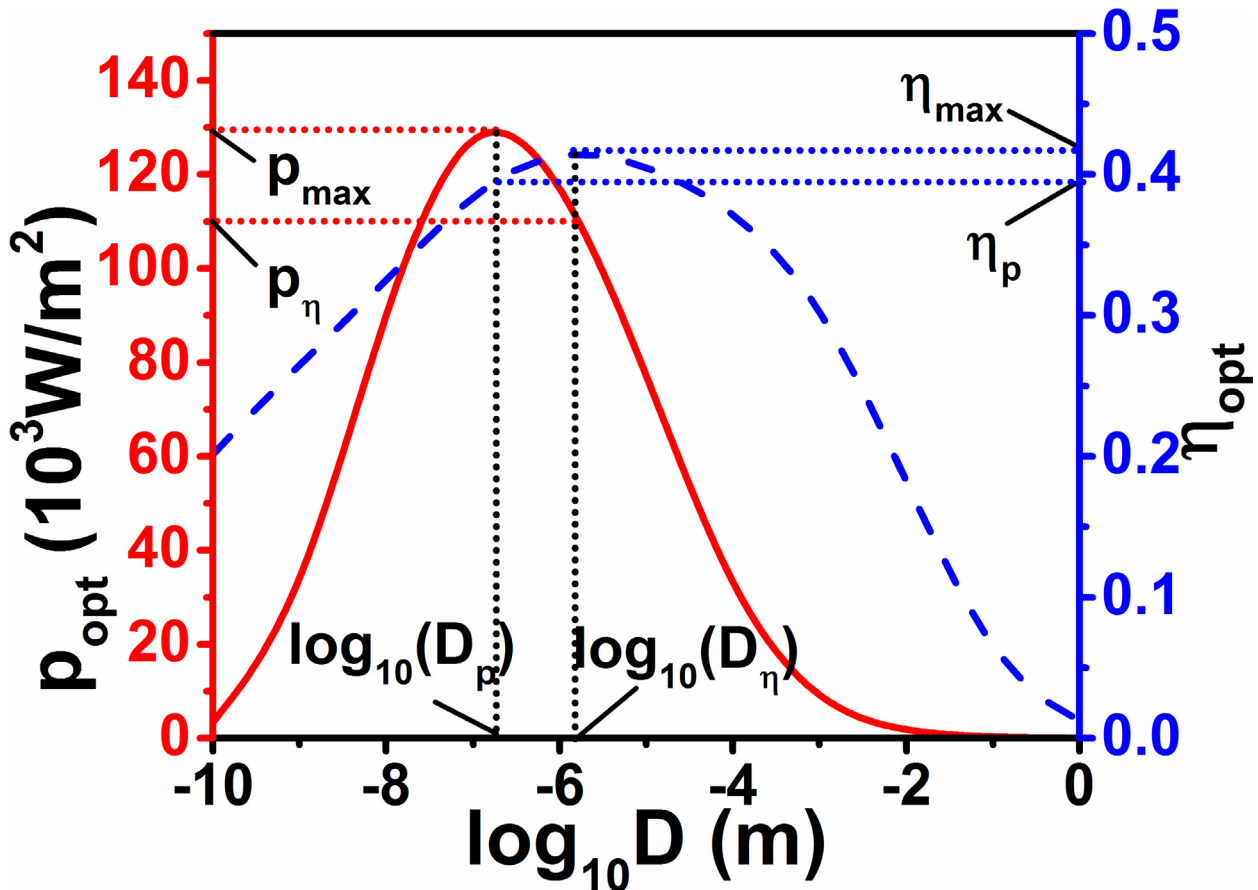


Fig. 5. p_{opt} and η_{opt} as functions of D , where J and x have been optimized.

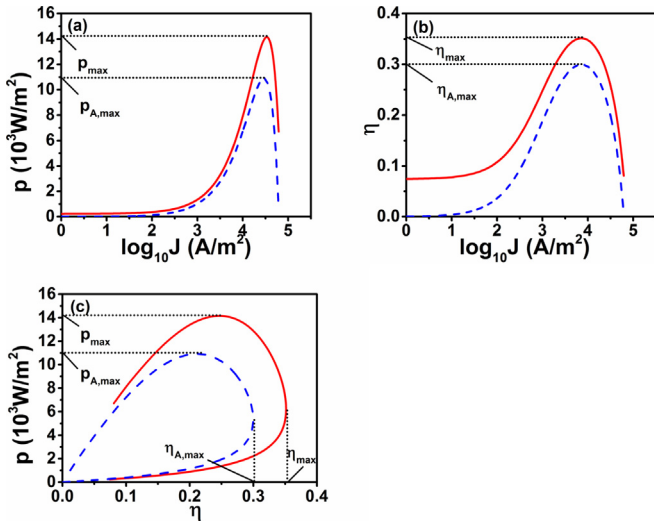


Fig. 7. The (a) $p \sim J$, (b) $J \sim \eta$, and (c) $\eta \sim p$ curves, where $D = 3.16 \times 10^{-4}$ and x has been optimized. The performances of the integrating system and AMTEC are, respectively, denoted by the red solid and blue dash lines denote.

seen from Fig. 5 that p_{opt} and η_{opt} firstly increase and then decrease with the increase of D . When $D = D_p$ and $D = D_\eta$, p_{opt} and η_{opt} attain their respective maxima, 1.30×10^5 W/m² and 0.425, respectively, which are significantly larger than those (1.42×10^4 W/m² and 0.352) obtained for the representative D value in Fig. 3. According to Fig. 5, the optimum range of D is given by

$$D_p \leq D \leq D_\eta. \quad (20)$$

Eq. (A4) indicates clearly that T_C is dependent on D . For the different values determined by Eq. (20), T_C has different optimum values, as shown in Fig. 6 (a), where $T_{C,p}$ and $T_{C,\eta}$ are the upper and lower boundaries of the optimum values of T_C . Note that $T_{C,p}$ is not marked in Fig. 6 (a) because it is higher than 800 K, which is the upper boundary of the condenser temperature. In the temperature range 400–800 K of the condenser temperature, Eq. (20) should be changed as

$$D_0 \leq D \leq D_\eta, \quad (21)$$

As shown in Fig. 6 (a), where D_0 is the D value corresponding to the upper temperature 800 K of the condenser temperature. According to Eq. (21), Fig. 6(b)–(d) show the effects of D on c_c/A_E , J , and x , where $(c_c/A_E)_p$ and $(c_c/A_E)_\eta$ and J_p and J_η are the upper and lower boundaries of c_c/A_E and J , and x_0 and x_η correspond to the cases of $D = D_0$ and $D = D_\eta$, respectively. According to Eqs. (18), (19) and (21), one can obtain that the optimal regions of c_c/A_E and J are, respectively, indicated by the gray areas in Fig. 6(b) and (c), and the optimal range of x is given by $x_0 \geq x \geq x_\eta$. According to Eq. (10) and Fig. 6 (d), one can gain the optimal range of the pressure ratio r_p in the heat engine as $3.58 \geq r_p \geq 2.66$. Such pressure ratios are typical of irreversible Brayton arrangements with a compressor and one turbine incorporating a regenerative process to preheat the working fluid entering the combustion chamber (Horlock, 2003; Cheng, 1999; Zhang et al., 2006; Sánchez-Orgaz et al., 2010).

4. Discussion

In order to expound further the advantages of the AMTEC-BHE integrating system, the optimum performance characteristic curves of the integrating system will be compared with those of the

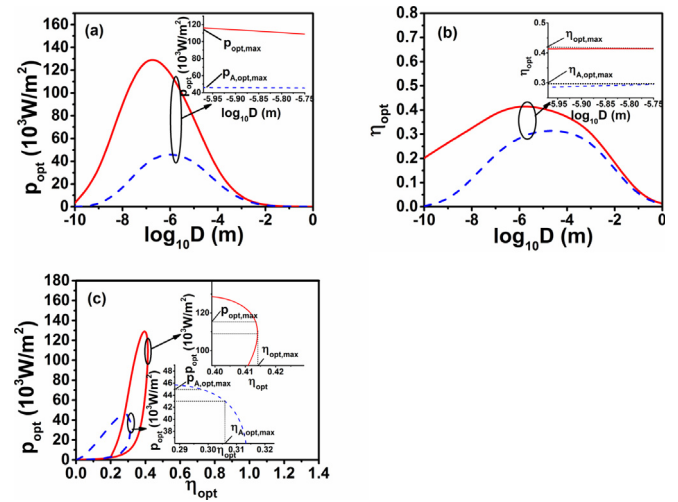


Fig. 8. The (a) $D \sim p_{opt}$, (b) $D \sim \eta_{opt}$, and (c) $\eta_{opt} \sim p_{opt}$ curves, where x and J has been optimized. The performances of the integrating system and the AMTEC are, respectively, denoted by the red solid and blue dash lines.

AMTEC. By using Eqs. 15 and 16, and (A1)–(A4), the POD and efficiency of the integrating system and AMTEC can be calculated for different values of J , as indicated in Fig. 7(a) and (b), where $D = 3.16 \times 10^{-4}$ m and the optimized values of x in the integrating system has been chosen. Fig. 7(a) and (b) show that there are a MPOD $p_{A,max}$ W/m² and a ME η_{max} for the integrating system, while the MPOD and ME of the AMTEC system working alone are, respectively, $p_{A,max}$ W/m² and $\eta_{A,max}$. These advantages of the AMTEC-BHE integrating system for a given D -value are better visualized in Fig. 7 (c), where it can be seen that the $\eta \sim p$ curve of the AMTEC is enveloped in that of the integrating system.

For different values of D , the POD and efficiency of the integrating system and AMTEC are displayed in Fig. 8, where the optimized values of x and J are chosen for the different values of D . Fig. 8 shows clearly that the POD and efficiency of the AMTEC are smaller than those of the integrating system for an arbitrary value of D . According to Eq. (21), when $D = D_0$, the integrating system attain their respective MPOD and ME, i.e., 1.16×10^5 W/m² and 0.417, which increase about 158% and 44.8%, compared with the MPOD and ME of the AMTEC. It is very significant that the ME of the proposed model increases about 33.2% and 20.5% compared with that of the AMTEC-TEG systems operating at optimum states (Wu et al., 2017; Peng et al., 2019a), respectively. These facts show that the construction of the proposed model is special meaning as the exhaust heat generated by the AMTEC can be available utilized by the BHE.

To end this section, in Table 2 we summarize some significant comparison for the obtained efficiencies and power outputs with previously reported results.

5. Multi-objective and multi-parametric optimization predictions

So far, we have studied the optimal problem of a single objective function such as the power output or the efficiency by using two control variables, J and x , and the coupling parameter D (directly linked to T_C). However, a global optimization could be realized if these three quantities are subject to a multi-objective optimization. This involves the simultaneous optimization of two objective functions, both p and η , in terms of three parameters (J , x , and D or T_C). The result is a set of values of these functions with the best compromise among them (from all possible physical values) and for

Table 2
Comparison of η_{max} and p_{max} in this work with previous reported results for the listed arrangements.

Systems	Parameters		η_{max} percentage increase compared with single AMTEC	p_{max} percentage increase compare with single AMTEC
	η_{max}	p_{max} ($10^3 W / m^2$)		
AMTEC-BHE (this paper)	0.417	116	44.8%	158%
AMTEC (Peng et al., 2018)	0.220	7.04	–	–
AMTEC-AR (Wang et al., 2019)	0.392	–	47.7%	–
AMTEC-TEG (Wu et al., 2017)	0.313	–	14.3%	–
AMTEC-TEG (Peng et al., 2019a)	0.346	64.3	9.15%	34.0%
Solar-AMTEC (Peng et al., 2019b)	0.211	48.0	–	–

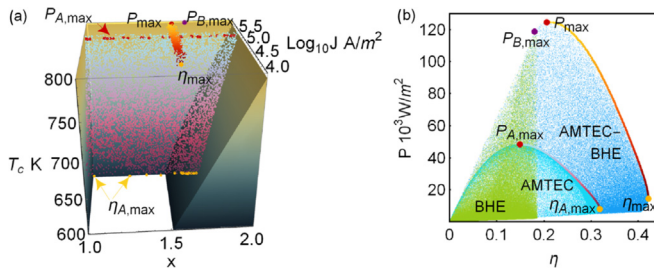


Fig. 9. (a) Parameter space bounded by the depicted surface indicating the region of physical interest. From all possible physical configurations, those leading to the optimum compromise between the maximum power and the maximum efficiency for both subsystems and the integrating system are depicted. (b) Energetic representation in the η - p space showing the Pareto front.

which a further improvement in one function involves the degrading to the rest. Along with these values (in the optimization function space) there is a set corresponding to the configuration leading to them in the values of the optimization variables and parameters so that they form the Pareto optimal set. Details of how to compute them can be found in Ref. (Tournier and El-Genk, 1999) and the implementation using genetic algorithms (not needed in this case due to absence of local minima values) can be found in Refs. (Spence et al., 2003; Deb, 2001).

The acceptable physical values for J , x , and D are such that T_C is in the interval from 400 to 800 K, and η_A , η_B , η , P_A , P_B and P are all positive quantities. In order to compare the optimization of each subsystem and the overall system, the multi-objective optimization is done for the three configurations. This region is depicted in Fig. 9 (a) for the isolated BHE, isolated AMTEC, and coupled AMTEC-BHE system. A random search in this physical region produces a first generation of points in the η - p space. These are mapped into the energetic space as depicted in Fig. 9 (b). The results in each case are displayed in both subfigures; in the variable space the Pareto optimal set and in the energetic space the Pareto front. Notice that in the case of the BHE subsystem, because of the limited range of x (and r_p values) it is no possible to find an optimum configuration for power and efficiency. On the other hand, the solely configuration of the AMTEC has clearly a compromise region between maximum power (outside of the physical region, as previously discussed) and a maximum efficiency.

In the previous sections of the manuscript, the values of the current J and temperature T_C (linked to D) were considered in the range where the AMTEC subsystem performance is optimum. However, the results for the integrating system indicates a preference for a narrow region for the x values, high temperature $T_C = 800$ K and large current J . In this way, there is a noticeable improvement of the efficiency and power output. Such configuration indicates that, in the coupling with other subsystems, the AMTEC design should be modified no to operate in its optimum configuration, but with a small variation leading to an overall

improvement. In particular, it is stressed how power and efficiency could get improvements of power up to almost 33% and efficiency up to almost 25% in the optimization of the overall system.

6. Summary and conclusions

In summary, a novel model of the hybridized AMTEC-BHE power system has been presented by including the main external and internal losses of subsystems. The matching problem between the AMTEC and the BHE has been tackled and the results earned here may contribute to the development of efficient AMTEC-BHE hybrid systems. The three most relevant results could be listed as follow:

- (i) The different influence of main key parameters on the overall system performance (such as pressure ratio of the Brayton cycle and the corresponding isentropic efficiencies, the thickness of the electrolyte, and the current density of the AMTEC) have been discussed and the optimized upper and lower bounds of the POD and efficiency are obtained.
- (ii) The energetic performance of the AMTEC-BHE system is better than that of the AMTEC at any thickness of the electrolyte: In particular, the MPOD and ME of the integrating system increase about 158% and 44.8% compared with those of the AMTEC. Besides, the energetic advantages of the integrating system are greater than those of other coupling systems such as AMTEC-TEG systems. See Table 2 for a comparison among different results and strategies.
- (iii) The multi-objective and multi-parametric optimization analysis based on the Pareto front and space of states physically acceptable shows that the configuration of optimum performance for the AMTEC working alone matches partially the optimum performance for the AMTEC-BHE system, for which a greater performance would be available assuming small different values of the design parameters.

Finally, it is worth mention that the study here presented is amenable to a further extension to consider different solarized and hybrid arrangements of an AMTEC plant in order to analyze its performance and feasibility under renewable energy inputs. Work along this line is currently in progress.

Declaration of competing interest

We declare that we have no financial and personal relationships with other people or organizations that can inappropriately influence our work, there is no professional or other personal interest of any nature or kind in any product, service and/or company that could be construed as influencing the position presented in, or the review of, the manuscript entitled.

CRedit authorship contribution statement

Wanli Peng: Conceptualization, Methodology, Software, Formal analysis, Writing - original draft, Writing - review & editing. **Julian Gonzalez-Ayala:** Software, Formal analysis, Writing - review & editing. **Juncheng Guo:** Validation, Formal analysis, Visualization. **Jincan Chen:** Resources, Conceptualization, Writing - review & editing, Supervision, Data curation, Funding acquisition. **Antonio Calvo Hernández:** Resources, Conceptualization, Writing - review & editing, Supervision, Data curation, Funding acquisition.

Acknowledgments

This work has been supported by the National Natural Science Foundation of China (No. 11675132), People's Republic of China and China Scholarship Council (CSC) under the State Scholarship Fund (No. 201806310020), People's Republic of China, and Junta de Castilla y Leon under project SA017P17. J.G.A. acknowledges Universidad de Salamanca contract 2017/X005/1. In addition, Wanli Peng thanks all members of the thermodynamics research group at the University of Salamanca for the help they provided during her stay.

Appendix A. The voltage output can be displayed as

$$V = \frac{RT_H}{F} \ln[1 + p_{sat}(T_H)\mu D / (RT_H)] - V_{ac} - V_R, \quad (A1)$$

where $p_{sat}(T) = 10^{9.678 - 5383.2/T}$ is the saturation vapor pressure at temperature T (Lodhi et al., 2001), μ indicates a electrolyte coefficient, D denotes the thickness of the electrolyte, R indicates gas constant, over potential difference V_{ac} and ionic BASE voltage V_R can be, respectively, written as (Wu et al., 2010; Lodhi et al., 2001; Gonzalez-Ayala et al., 2019)

$$\begin{aligned} V_{ac} = & -\frac{2RT_H}{F} \ln \left[\frac{1}{2} \left[\frac{J^2 T_H}{B^2 p_{sat}^2(T_H)} + 4 \right]^{\frac{1}{2}} - \frac{1}{2} \frac{J\sqrt{T_H}}{B p_{sat}(T_H)} \right] \\ & + \frac{2RT_H}{F} \ln \left[\frac{1}{2} \left[\frac{J^2 \sqrt{T_H T_C}}{B^2 p_{sat}(T_H) p_{sat}(T_C)} \right. \right. \\ & \left. \left. + 4 \left[1 + \frac{\Delta p_{cd} \sqrt{T_C}}{p_{sat}(T_C) \sqrt{T_H}} \right] \right]^{\frac{1}{2}} + \frac{1}{2} \frac{J(T_H T_C)^{\frac{1}{4}}}{B \sqrt{p_{sat}(T_H) p_{sat}(T_C)}} \right], \quad (A2) \end{aligned}$$

and

$$\begin{aligned} V_R = & JD \left[1.62 \times 10^{-5} T_H \exp(-45.5 / T_H) \right. \\ & \left. + 1.55 \times 10^{-7} T_H \exp(3722 / T_H) \right], \quad (A3) \end{aligned}$$

where B indicates the charge-exchange coefficient, G denotes the pressure losses geometric factor, and the pressure loss Δp_{cd} is equal to $\left(1 + \frac{3G}{8\pi}\right) \sqrt{2\pi MRT_H} \frac{I}{F}$ (Tournier et al., 1997; Sánchez-Orgaz et al., 2015). It is worthwhile noting that T_C is depends on some

parameters such as T_H , μ and D . The specific relational expression is given by Peng et al. (2018)

$$\frac{p_{sat}(T_H)}{1 + p_{sat}(T_H)\mu D / (RT_H)} = p_{sat}(T_C) \sqrt{\frac{T_H}{T_C}}. \quad (A4)$$

References

- Bontempo, R., Manna, M., 2019. Work and efficiency optimization of advanced gas turbine cycle. *Energy Convers. Manag.* 195, 1255–1279.
- Cheng, C.Y., 1999. Ecological optimization of an irreversible Brayton heat engine. *J. Phys. D Appl. Phys.* 32, 350.
- Durante, A., Pena-Vergara, G., Curto-Risso, P.L., Medina, A., Hernández, A.C., 2017. Thermodynamic simulation of a multi-step externally fired gas turbine powered by biomass. *Energy Convers. Manag.* 140, 182–191.
- Deb, K., 2001. Multi-objective Optimization Using Evolutionary Algorithms, vol. 16, 978-0-471-87339-6.
- El-Genk, M.S., Tournier, J.M., 2002. Performance comparison of potassium and sodium vapor anode, multi-tube AMTEC converters. *Energy Convers. Manag.* 43, 1931–1951.
- González-Portillo, L.F., Muñoz Antón, J., Martínez Val, J., 2019. Thermodynamic mapping of power cycles working around the critical point. *Energy Convers. Manag.* 192, 359–373.
- Gonzalez-Ayala, J., Guo, J., Medina, A., Roco, J.M.M., Hernández, A.C., 2019. Optimization induced by stability and the role of limited control near a steady state. *Phys. Rev. E* 100, 0621128.
- Guo, J., Cai, L., Chen, J., Zhou, Y., 2016. Performance evaluation and parametric choice criteria of a Brayton pumped thermal electricity storage system. *Energy* 113, 693–701.
- Horlock, J.H., 2003. *Advanced Gas Turbine Cycles*. Pergamon Press.
- Lodhi, M.A.K., Daloglu, A., 2000. Effect of geometrical variations on AMTEC cell heat losses. *J. Power Sources* 91, 99–106.
- Lodhi, M.A.K., Vijayaraghavan, P., Daloglu, A., 2001. An overview of advanced space/terrestrial power generation device: AMTEC. *J. Power Sources* 103, 25–33.
- Peng, W., Zhang, X., Ye, Z., Chen, J., 2018. Optimum operation states and parametric selection criteria of an updated alkali metal thermal electric converter. *Energy Convers. Manag.* 168, 230–236.
- Peng, W., Li, W., Ye, Z., Su, G., Chen, J., 2019a. Parametric design strategies of an updated alkali metal thermoelectric converter-thermoelectric generator system operating at optimum states. *Energy Convers. Manag.* 182, 53–59.
- Peng, W., Li, W., Chen, X., Su, G., Chen, J., 2019b. Optimum operation states and parametric selection criteria of an updated solar-driven AMTEC. *Renew. Energy* 141, 209–216.
- Sánchez-Orgaz, S., Medina, A., Hernández, A.C., 2010. Thermodynamic model and optimization of a multi-step irreversible Brayton cycle. *Energy Convers. Manag.* 51, 2134–2143.
- Sánchez-Orgaz, S., Pedemonte, M., Ezzatti, P., Curto-Risso, P.L., Medina, A., Hernández, A.C., 2015. Multi-objective optimization of a multi-step solar-driven Brayton plant. *Energy Convers. Manag.* 99, 346–358.
- Santos, M.J., Merchan, R.P., Medina, A., Hernández, A.C., 2016. Seasonal thermodynamic prediction of the performance of a hybrid solar gas-turbine power plant. *Energy Convers. Manag.* 115, 89–102.
- Spence, C.A., Schuller, M., Lalk, T.R., 2003. Development, evaluation, and design applications of an AMTEC converter model. *AIP Conf. Proc.* 654, 685–700.
- Tournier, J.M., El-Genk, M.S., Schuller, M., Hausgen, P., 1997. An analytical model for liquid-anode and vapor-anode AMTEC converters. *AIP Conf. Proc.* 387, 1543–1552.
- Tournier, J.M., El-Genk, M.S., 1999. An electric model of a vapour anode, multitube alkali-metal thermal-to-electric converter. *J. Appl. Electrochem.* 29, 1263–1275.
- Underwood, M.L., Williams, R.M., Ryan, M.A., Jeffries-Nakamura, B., O'Connor, D., 1992. An AMTEC vapor-vapor, series connected cell. *AIP Conf. Proc.* 246, 1331–1337.
- Wang, Y., Zhang, H., Hao, H., Li, H., 2019. Performance assessment and parametric study of a hybrid system consisting of an alkali metal thermoelectric converter and an absorption refrigerator. *Energy Convers. Manag.* 188, 346–353.
- Wu, S.Y., Xiao, L., Cao, Y., Li, Y.R., 2010. A parabolic dish/AMTEC solar thermal power system and its performance evaluation. *Appl. Energy* 87, 452–462.
- Wu, S.Y., Guo, G., Xiao, L., Chen, Z.L., 2019. A new AMTEC/TAR hybrid system for power and cooling cogeneration. *Energy Convers. Manag.* 180, 206–217.
- Wu, S.Y., Zhang, Y.C., Yang, H., Xiao, L., 2017. Performance evaluation and parametric analysis of AMTEC/TEG hybrid system. *Energy Convers. Manag.* 154, 118–126.
- Wu, S.Y., Zhang, Y.C., Xiao, L., 2018. Conceptual design and performance analysis of concentrated solar-driven TIC/AMTEC/TEG hybrid system. *Int. J. Energy Res.* 42, 4674–4686.
- Zhang, Y., Ou, C., Lin, B., Chen, J., 2006. The regenerative criteria of an irreversible Brayton heat engine and its general optimum performance characteristics. *J. Energy Resour. Technol.* 128, 216–222.